

# Influence of resonant plasmonic nanoparticles on optically accessing the valley degree of freedom in 2D semiconductors

Tobias Bucher,<sup>\*,†,‡,¶,△</sup> Zlata Fedorova,<sup>\*,†,‡,¶,△</sup> Mostafa Abasifard,<sup>‡,†,¶</sup>  
Rajeshkumar Mupparapu,<sup>‡,¶</sup> Matthias J. Wurdack,<sup>§,†,‡,¶</sup> Emad Najafidehaghani,<sup>||</sup>  
Ziyang Gan,<sup>||</sup> Heiko Knopf,<sup>⊥,‡,¶,#</sup> Antony George,<sup>||,¶</sup> Falk Eilenberger,<sup>⊥,‡,¶,#</sup>  
Thomas Pertsch,<sup>‡,¶,⊥,#</sup> Andrey Turchanin,<sup>||,¶,@</sup> and Isabelle Staude<sup>†,‡,¶,#</sup>

<sup>†</sup>*Institute of Solid State Physics, Friedrich Schiller University Jena, 07743 Jena, Germany*

<sup>‡</sup>*Institute of Applied Physics, Friedrich Schiller University Jena, 07745 Jena, Germany*

<sup>¶</sup>*Abbe Center of Photonics, Friedrich Schiller University Jena, 07745 Jena, Germany*

<sup>§</sup>*ARC Centre of Excellence in Future Low-Energy Electronics Technologies and Department of Quantum Science and Technology, Research School of Physics, The Australian National University, Canberra, ACT, 2601, Australia*

<sup>||</sup>*Institute of Physical Chemistry, Friedrich Schiller University Jena, 07743 Jena, Germany*

<sup>⊥</sup>*Fraunhofer Institute for Applied Optics and Precision Engineering IOF, 07745 Jena, Germany*

<sup>#</sup>*Max Planck School of Photonics, Germany*

<sup>@</sup>*Jena Center for Soft Matter (JCSM), 07743 Jena, Germany*

<sup>△</sup>*These authors contributed equally*

E-mail: tobias.bucher@uni-jena.de; zlata.fedorova@uni-jena.de

## Abstract

The valley degree of freedom is one of the most intriguing properties of atomically thin transition metal dichalcogenides. Together with the possibility to address this degree of freedom by valley-contrasting optical selection rules, it has the potential to enable a completely new class of future electronic and optoelectronic devices. Resonant optical nanostructures emerge as promising tools for interacting with and controlling the valley degree of freedom at the nanoscale. However, a critical understanding gap remains in how nanostructures and their nearfields affect the polarization properties of valley-selective chiral emission hindering further developments in this field. In order to address this issue, our study delves into the experimental investigation of a hybrid model system where valley-specific chiral emission from a monolayer of molybdenum disulfide is interacting with a resonant plasmonic nanosphere. Contrary to the simple intuition suggesting that a centrosymmetric nanoresonator preserves the degree of circular polarization in the farfield, our cryogenic photoluminescence microscopy reveals almost complete depolarization. We rigorously study the nature of this phenomenon numerically considering the monolayer-nanoparticle interaction at different levels including excitation and emission. In doing so, we find that the farfield degree of polarization strongly reduces in the hybrid system when including excitons emitting from outside of the system's symmetry point, which in combination with depolarisation at the excitation level causes the observed effect. Our results highlight the importance of considering spatially distributed chiral emitters for precise predictions of polarization responses in these hybrid systems. This finding advances our fundamental knowledge of the light-valley interactions at the nanoscale but also unveils a serious impediment of the practical fabrication of resonant valleytronic nanostructures.

## Introduction

As modern CMOS-based information technology is facing fundamental limits of further downscaling, novel materials providing additional electronic degrees of freedom, such as

spin or valley-pseudospin, have become an active topic of research<sup>1-6</sup>. The valley-pseudospin arises from multiple degenerate but inequivalent energy extrema in the bands of a crystal, in which excitons with distinct spin states can form that may be used to encode and process information<sup>7-9</sup>. In two-dimensional transition metal dichalcogenides (2D-TMDs), the broken inversion symmetry of the crystal structure and strong spin-orbit coupling lead to spin-valley locking and consequently valley-contrasting optical selection rules. Following this valley-degree of freedom, energy-degenerate excitons with opposite spin are located at the K or K' points (or valleys) at the corners of the Brillouin zone.<sup>10-12</sup> The pronounced direct bandgap photoluminescence (PL) in the monolayer phase,<sup>13,14</sup> facilitates efficient addressing and readout of the valley-degree of freedom in 2D-TMDs using circularly polarized light. However, the robust detection, manipulation and transport of the valley-pseudospin information is still challenging, mainly because of the short lifetime of valley-polarized excitonic states.

During the last few years, the integration of 2D-TMDs with photonic nanostructures has gained immense popularity as an approach to address this challenge. For instance, chiral photonic nanostructures have been proven to selectively enhance and efficiently tailor emission from individual valleys.<sup>15-19</sup> Coupling 2D-TMDs to achiral dielectric metasurfaces demonstrated potential in controlling directionality, lifetime, and spectral shape of the PL response.<sup>20,21</sup> Other nanophotonic structures facilitated the generation of valley-polarized plasmon/photon-exciton polaritons opening new ways for valley control.<sup>22,23</sup> However, of crucial importance for the development of on-chip valleytronic devices is directional routing of the valley-pseudospin information. Routing has been reported in structures supporting guided modes with spin-momentum locking<sup>2,3,22,24</sup> and photonic crystals.<sup>25,26</sup> Despite these advancements, an apparent lack of experimental progress remains in the manipulation of valley-selective emission at the level of single nanoantennas. A notable divergence is observed in this context: The experimentally observed effects, though valuable, fell short of the expected efficiency in numerical simulations.<sup>16</sup> Additionally, other nanophotonic designs

require the employment of electron beam excitation techniques,<sup>27,28</sup> which significantly increases the technical complexity as well as the costs of the proposed schemes. Demonstrating efficient schemes for nanoantenna-based valley-routing employing widely accessible and integratable optical techniques therefore remains an open challenge.

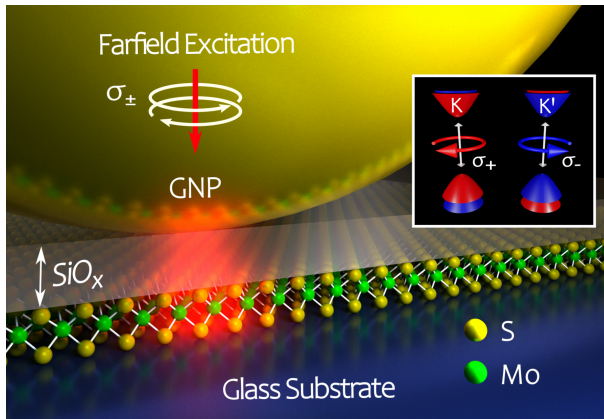


Figure 1: Schematic of the investigated hybrid model excited by circularly polarized light. A resonant gold nanoparticle (size 200 nm) is placed above a monolayer of molybdenum disulfide situated on a glass substrate. A thin dielectric spacer layer of silicon oxide (thickness 15 nm) was introduced prior to the nanoparticle deposition in order to prevent direct metal-TMD contact. Note that the crystal structure was scaled up for better visibility. The inset figure illustrates the valley-contrasting optical selection rules in monolayer TMDs.

As the investigated nanophotonic architectures gain in complexity, the crucial prerequisite of precisely modelling the electromagnetic interaction between the valley-selective chiral emitters and the resonant modes of these nanostructures becomes challenging and poses a limitation for further developments in this field. In light of this, we investigate a simplified model system as sketched in Figure 1. Namely, we focus on a spherically symmetric (and hence achiral) single gold nanoparticle (GNP) resonantly interacting with valley-specific chiral emission from a monolayer of molybdenum disulfide (1L-MoS<sub>2</sub>). By performing polarization-resolved cryogenic PL microscopy, we study the farfield polarization properties of this hybrid system under circularly-polarized optical pumping. Although it seems intuitive that an achiral nanoantenna should not affect the valley-pseudospin as it equally interacts with both K and K' valleys, we observe robust quenching of the degree of circular polariza-

tion in the farfield.

We compare our findings with a systematic numerical analysis of both excitation and emission aspects of the conducted experiments. We thereby isolate the main mechanisms that govern the observed depolarization. In particular, we find that the degree of circular polarization drops dramatically once the excitons are positioned only a few tens of nanometers away from the symmetry point leading to complete depolarization after averaging over contributions from excitons within the optical resolution limit. With this work, we not only aim to refine the existing simulation approaches for valleytronic devices, but also contribute to the deeper understanding of the rich physics of light-valley interactions at the nanoscale.

## Sample preparation

We prepared hybrid nanoparticle-on-substrate structures incorporating embedded 1L-MoS<sub>2</sub> by means of a simple spin-coating scheme (see Methods for a detailed description of all processes). Initially, we synthesized 1L-MoS<sub>2</sub> by chemical vapour deposition (CVD) on silicon/silicon-dioxide wafers<sup>29</sup>. The growth process yields a dense coverage of the substrate with high-optical quality 1L-MoS<sub>2</sub> crystals<sup>30</sup> reaching edge lengths of up to 60  $\mu\text{m}$ . Next, we transferred the as-grown 1L-MoS<sub>2</sub> crystals onto a glass wafer by polymethylmethacrylate assisted wet-transfer<sup>31</sup>. Subsequently, we coated the sample with 15 nm silicon oxide using an optimized physical vapour deposition process<sup>32</sup>. The dielectric spacer layer prevents charge-transfer induced quenching of emission from 1L-MoS<sub>2</sub> by avoiding direct contact with the GNPs. Finally, by drop-casting and subsequent spin-coating we sparsely distributed monodispersed GNPs with an average size of  $(220 \pm 15)$  nm on top of the prepared substrates. Figure 2a and Figure 2b show an optical bright-field and dark-field microscope image, respectively, of a typical sample. The embedded 1L-MoS<sub>2</sub> crystals are decorated by several monodispersed GNPs which are visible in both images as bright spots as indicated by circles. Next, we characterized the optical properties of the prepared sample at cryogenic

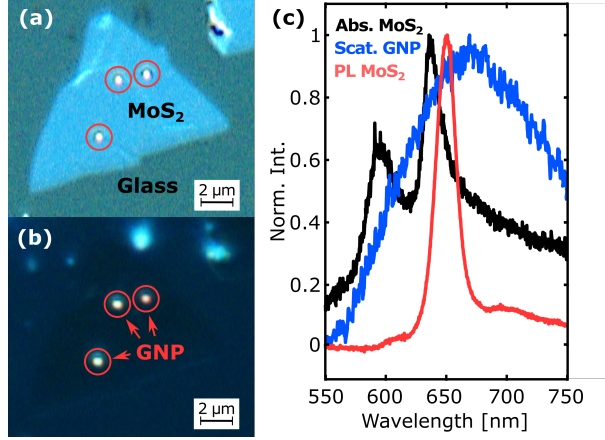


Figure 2: (a) Optical brightfield and (b) darkfield microscope image of a prepared substrate incorporating embedded 1L-MoS<sub>2</sub> crystals and being decorated by several GNPs. The red circles indicate the positions of GNPs lying atop an embedded 1L-MoS<sub>2</sub> crystal. (c) Measured cryogenic ( $T = 3.8$  K) white light absorption (black curve) and PL (red curve) spectrum of an embedded 1L-MoS<sub>2</sub> crystal as well as the white light reflection spectrum of an isolated GNP (blue curve).

temperature as shown in Figure 2c (see Methods). The white light absorption spectrum (black curve) of the embedded 1L-MoS<sub>2</sub>, which was measured with a tungsten-halogen white light source, shows two distinct peaks at 645 nm and 595 nm wavelength which are related to the A- and B-excitonic resonances formed at the direct bandgap in the K/K' points of the Brillouin zone. The pronounced absorption peaks indicate a large oscillator strength of the A- and B-excitons formed in our samples showing the high-optical quality of the embedded 1L-MoS<sub>2</sub>. In this study, we focus on the emission from the embedded 1L-MoS<sub>2</sub> which is dominated by the lower-energetic A-exciton as shown in the PL spectrum as measured from the same sample (red curve). The observed PL peak centered at 650 nm wavelength is slightly Stokes-shifted with respect to the A-exciton absorption peak and has a line width of about 60 meV which is comparable to the values of as-grown 1L-MoS<sub>2</sub> from our previous work<sup>30</sup> indicating the non-degradative character of the silicon oxide deposition process. We further verified the resonant character of the deposited GNPs at the central emission wavelength of the embedded 1L-MoS<sub>2</sub> crystals by measuring its white light reflectivity spectrum (blue curve). The GNP exhibits an electric dipolar resonance visible as broad peak centered at

670 nm wavelength. Despite a slight red-shift of the GNP reflectivity spectrum with respect to the A-exciton energy of the embedded 1L-MoS<sub>2</sub> crystals, the broad width of the plasmonic resonance provides sufficient spectral overlap.

## Polarization-resolved cryo-PL measurements

We investigated the modification of the farfield degree of circular polarization (DOCP) of valley-specific chiral emission from 1L-MoS<sub>2</sub> when scattered by a resonant GNP by performing polarization-resolved PL imaging at cryogenic temperature  $T = (3.8 \pm 0.1)$  K. To achieve valley-selective excitation of excitons, we pumped the sample near-resonantly at 633 nm wavelength and with  $\sigma^+$  polarization. For excitation and detection we used a 100x/0.9 NA objective in reflection geometry and limited the collected light to a  $(660 \pm 5)$  nm wavelength band (see Methods). We further analyzed the collected light in a helical basis ( $\sigma^\pm$ ) to obtain the valley-specific emission intensities ( $\mathcal{I}_{\sigma^\pm}$ ) and calculated the farfield DOCP as  $\text{DOCP} = (\mathcal{I}_{\sigma^+} - \mathcal{I}_{\sigma^-}) / \mathcal{I}_{\text{tot}}$  where  $\mathcal{I}_{\text{tot}} = (\mathcal{I}_{\sigma^+} + \mathcal{I}_{\sigma^-})$  is the total emission intensity. In order to investigate the modification of the farfield DOCP of emission from embedded 1L-MoS<sub>2</sub> by the resonant GNP, we measured  $\mathcal{I}_{\sigma^\pm}$  as a function of position by confocal scanning microscopy as shown in Figure 3a. For both  $\mathcal{I}_{\sigma^+}$  and  $\mathcal{I}_{\sigma^-}$ , we observe a uniform distribution

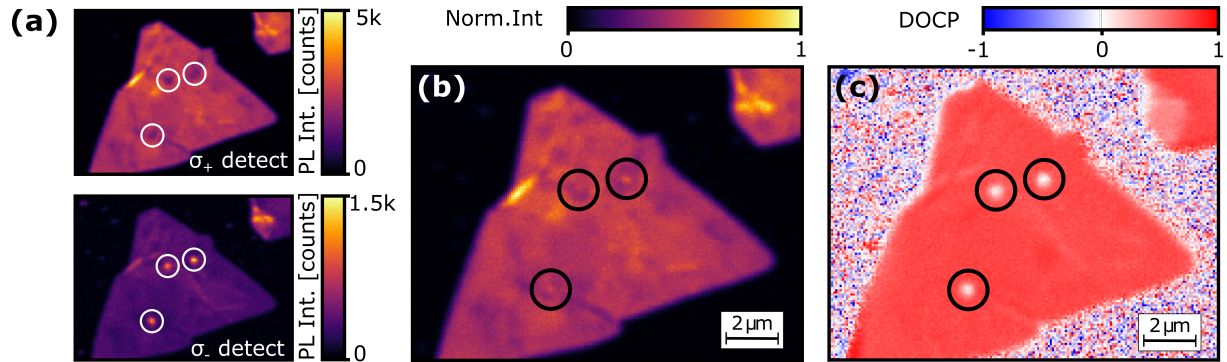


Figure 3: (a) Measured confocal scans of valley-specific emission intensities  $\mathcal{I}_{\sigma^\pm}$  from embedded 1L-MoS<sub>2</sub> decorated with monodispersed GNPs upon  $\sigma^+$  excitation and collected through a 660 nm bandpass filter. (b) Total intensity  $\mathcal{I}_{\text{tot}} = (\mathcal{I}_{\sigma^+} + \mathcal{I}_{\sigma^-})$  and (c) degree of circular polarization  $\text{DOCP} = (\mathcal{I}_{\sigma^+} - \mathcal{I}_{\sigma^-}) / \mathcal{I}_{\text{tot}}$  scans as calculated from the results shown in (a).

across the embedded 1L-MoS<sub>2</sub> crystal area where  $\mathcal{I}_{\sigma^+}$  is about 6-times higher than  $\mathcal{I}_{\sigma^-}$  as a signature of the induced exciton valley-polarization due to the valley-selective excitation. A different situation, however, is observed at the positions of the GNPs which are highlighted by circles. We find a significant local modulation of the valley-specific emission intensities with  $\mathcal{I}_{\sigma^+}$  being slightly reduced and  $\mathcal{I}_{\sigma^-}$  being noticeably enhanced with respect to the case without GNPs. To further quantify this effect we calculated  $\mathcal{I}_{\text{tot}}$  and DOCP as shown in Figure 3b and Figure 3c, respectively. While there is only a small modulation of  $\mathcal{I}_{\text{tot}}$  by the GNPs, we observe a strong reduction  $\Delta_{\text{DOCP}} = 0.63 \pm 0.11$  from  $0.71 \pm 0.03$  for embedded 1L-MoS<sub>2</sub> without GNP to  $0.08 \pm 0.08$  with GNP. As confirmed by full-polarization resolved measurements, the emission from the embedded 1L-MoS<sub>2</sub> with GNP exhibits negligible linear polarization components (see Supporting Information). Hence, the observed reduction in the DOCP is equivalent to a reduction of the total degree of polarization which can be clearly attributed to the presence of the GNPs. Interestingly, the cylindrical symmetry of the nanoparticle-on-substrate geometry considered in this work would suggest a preserved DOCP of emission which is in stark contrast to our experimental observations. In the following, we systematically analyze aspects of excitation and emission in our hybrid system and compare them with predictions from numerical simulations which allows us to isolate the mechanism leading to the observed reduction in the DOCP.

The initial requirement to observe valley-specific chiral emission from 1L-MoS<sub>2</sub> is a valley-selective excitation. By selection rules, the excitation rate of carriers in valleys K and K' is proportional to the intensity of the  $\sigma^+$  and  $\sigma^-$  polarized components of the external fields, respectively. Therefore, in equilibrium the local exciton densities  $n_K(x, y)$  and  $n_{K'}(x, y)$  must be proportional to  $I_{\sigma^+}^{\parallel}(x, y)$  and  $I_{\sigma^-}^{\parallel}(x, y)$ , respectively, where the superscript  $\parallel$  points to the fact that only the tangential components of external fields will contribute to the excitation of the material.<sup>33</sup> Note that, throughout this manuscript,  $I$  quantifies nearfield intensities, while  $\mathcal{I}$  relates to farfield intensities. The induced degree of valley-polarization,  $\eta = (n_K - n_{K'}) / (n_K + n_{K'})$ , is therefore proportional to the 2D-DOCP, i.e. the DOCP of

the tangential components, of the excitation field. In order to analyze the influence of the GNP on the valley-selective excitation of 1L-MoS<sub>2</sub>, we numerically calculate the helical intensities,  $I_{\sigma^{\pm}}^{\parallel} \propto |E_{\sigma^{\pm}}^{\parallel}|^2$ , in a plane 15 nm below the GNP for a  $\sigma^+$ -polarized excitation beam. Figure 4a shows the respective total intensity (top row) and 2D-DOCP (bottom row) for a

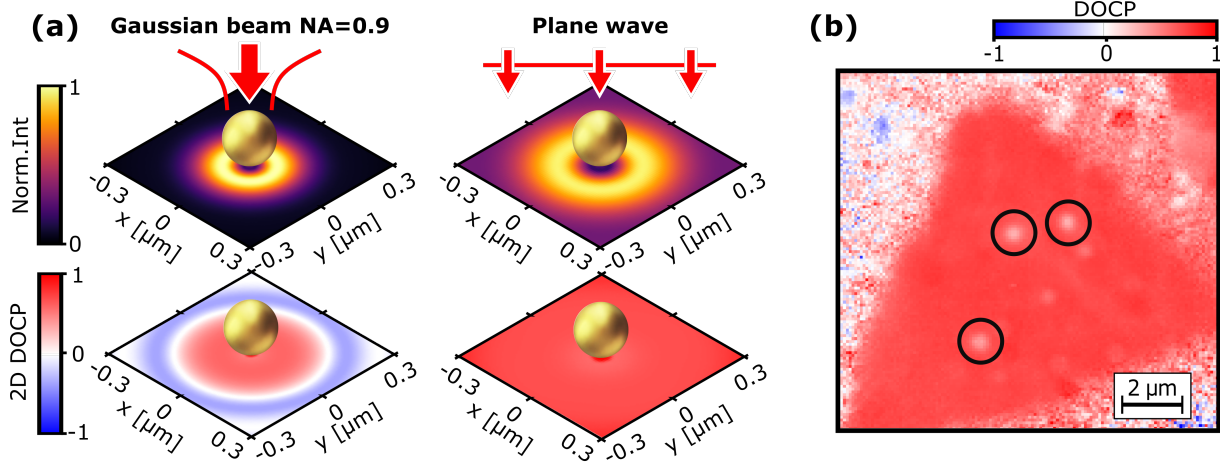


Figure 4: (a) Total intensity (top row) and DOCP (bottom row) of the external in-plane nearfield in the plane of the monolayer upon excitation with a focused Gaussian beam (NA=0.9) positioned at the center of the GNP (left) and a plane wave (right). (b) Measured DOCP of valley-specific emission from embedded 1L-MoS<sub>2</sub> decorated with monodispersed GNPs upon  $\sigma^+$ -polarized wide-field illumination and collected through a 660 nm bandpass filter.

focused Gaussian beam (left column) and a plane wave (right column). In both cases, the GNP leads to a slight reduction of the 2D-DOCP in its close vicinity, and thereby to a lower inducible degree of valley-polarization. Away from the projection point of the nanoparticle center, the impact of the GNP on the 2D-DOCP highly depends on the excitation scheme. For a tightly focused Gaussian beam (NA=0.9), the intensity drops rapidly outside of the focal spot and the total field is dominated by the scattered field. In fact, we observe a strong modification of the 2D-DOCP at larger distances even leading to field components of opposite helicity. For the case of a plane wave, the total field at larger distances from the GNP is dominated by the incident field, and we observe a unit 2D-DOCP as expected for a circularly polarized plane wave. Hence, the excitation scheme is expected to influence the observed reduction in DOCP of emission from 1L-MoS<sub>2</sub> mediated by the GNP. We therefore repeated

our cryo-PL imaging experiments using wide-field illumination (excitation-NA  $\approx 0$ ) mimicking the plane wave excitation. Figure 4b shows the respective measured DOCP image of PL from the same 1L-MoS<sub>2</sub> sample as shown before. Indeed, we observe a less pronounced local reduction of  $\Delta_{\text{DOCP}} = 0.39 \pm 0.06$  from  $0.72 \pm 0.02$  for embedded 1L-MoS<sub>2</sub> without GNP to  $0.33 \pm 0.04$  with GNP. While the lower  $\Delta_{\text{DOCP}}$  is qualitatively in line with the prediction from our nearfield simulations, the observed difference is, however, still significant. For a quantitative comparison of both excitation schemes on the basis of our numerical simulations, we need to take into account the finite optical resolution in our experiments. In case of the wide field scheme, we apply Gaussian smoothing to obtain the averaged helical excitation intensities  $\tilde{I}_{\sigma\pm}(x, y) \propto \iint G(\xi - x, \eta - y) I_{\sigma\pm}^{\parallel}(\xi, \eta) d\xi d\eta$ , where  $G(x, y)$  is a Gaussian weight function given by Equation 2 from the Methods section. For the confocal scanning scheme the resolution limit is encoded in the finite beam size. Importantly, during scanning the beam position relative to the GNP center changes. Therefore, the averaged helical excitation intensities at a distance  $r$  from the center of the GNP can be estimated as  $\tilde{I}_{\sigma\pm}(r) \propto \iint I_{\sigma\pm}^{\parallel}(r, \xi, \eta) d\xi d\eta$ , where  $I_{\sigma\pm}^{\parallel}(r, x, y)$  are the respective nearfield intensities resulting from the excitation with the focused beam that is displaced by the distance  $r$  from the GNP center. Finally, the numerically predicted farfield PL DOCP for each measurement setting is computed using Equation 4. We obtain a predicted reduction of  $\Delta_{\text{DOCP}} = 0.18 \pm 0.04$ , i.e. from  $0.72 \pm 0.02$  (measured) without to  $0.54 \pm 0.02$  (calculated) with GNP, and  $\Delta_{\text{DOCP}} = 0.45 \pm 0.06$ , i.e. from  $0.71 \pm 0.03$  (measured) without to  $0.26 \pm 0.03$  (calculated) with GNP, for the plane wave and Gaussian beam excitation, respectively. Our calculations based on excitation effects are consistent with the experimental observation of a larger reduction in DOCP for the case of the confocal as compared to the widefield excitation scheme. However, the experimentally observed changes of  $\Delta_{\text{DOCP}} = 0.39 \pm 0.06$  and  $\Delta_{\text{DOCP}} = 0.63 \pm 0.11$  remain systematically larger indicating additional contributing factors.

Note, that in this simple estimation we have not assumed any exciton diffusion which is known to potentially impact the electromagnetic interaction of emitters in 2D-TMDs with

optical nanoresonators<sup>34</sup>. In our system, however, we expect a rather weak impact of the nearfield of the GNP on the diffusion properties of the excitons in 1L-MoS<sub>2</sub> as first, we observe no significant modulation of the total cryo-PL intensity at the positions of the GNPs, and second, we find the depolarization effect to be robust across all our samples naturally including GNPs of slightly varying size and topography. Nevertheless, the observed DOCP of emission from 1L-MoS<sub>2</sub> with GNP cannot be explained by excitation effects alone but additional factors need to be considered as discussed next.

By symmetry, the nanoparticle-on-substrate geometry is expected to preserve the helicity of valley-selective chiral emission. This can be understood by modelling PL emission from dipoles exhibiting chiral farfield properties matching those of excitons in bare 1L-TMDs. For this purpose, different types of emitters with chiral farfield properties are discussed in literature with focus on their symmetry properties<sup>35–37</sup> or different multipolar coupling behaviour<sup>38,39</sup>. The prevalent model used in the context of 2D-TMDs is the rotating electric dipole<sup>2,3,5,17,21,22,28</sup>,  $\vec{p}_{K/K'} = \vec{p}_x \pm i\vec{p}_y$ , where the valley index is associated with the fixed phase sign.

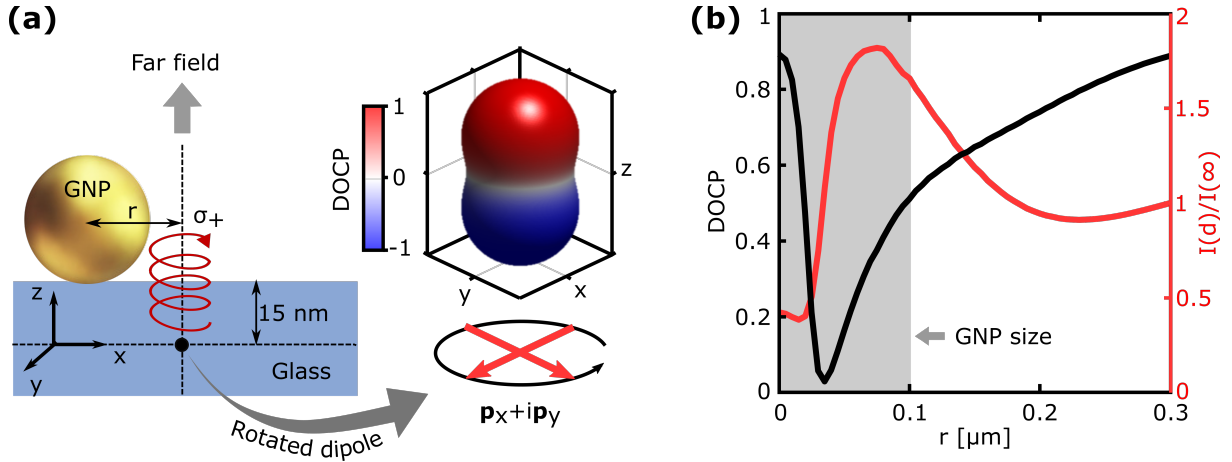


Figure 5: (a) Sketch of the simulated nanoparticle-on-substrate geometry showing the position of the rotating electric dipole in a plane 15 nm below and displaced by a distance  $r$  from the projected center of the GNP. The inset shows the calculated farfield radiation pattern of a rotating electric dipole  $\vec{p}_K$ , the color encodes the respective helicity. (b) Calculated DOCP (black curve) and intensity (red curve) of the integrated farfield emanating from the hybrid system as a function of displacement distance  $r$ . The farfield intensity is normalized to the intensity obtained without a GNP.

When placed below a resonant GNP, the rotating electric dipole is expected to induce a respective rotating mirror dipole of the same helicity (note that both linear dipole components of the mirrored rotating dipole are off-set by a  $\pi$  phase flip leaving the helicity unchanged). Consequently, the farfield distribution and DOCP of the hybrid system would be similar to the case of a bare rotating electric dipole as plotted on the right side of Figure 5a. However, this is only the case for a rotating dipole on the symmetry axis. For a finite displacement  $r > 0$  of the rotating dipole from the projected center of GNP, the cylindrical symmetry of the system is broken. To investigate the effect of the dipole displacement  $r$  on the farfield polarization of the hybrid system, we calculate the resulting farfield distribution for different emitter positions (see Methods). By integration over a numerical aperture of 0.9, we obtain the integrated helical farfield intensities  $\mathcal{I}_{\sigma\pm}(r)$ . In Figure 5b we show the resulting total farfield intensity (red curve) and the farfield DOCP (black curve) as functions of the displacement distance  $r$ . Here, the farfield intensity is normalized to the emission of a rotating electric dipole without GNP, i.e. at infinite distance. As expected from symmetry, we obtain a high farfield DOCP for dipoles below the center of the GNP ( $r = 0$ ). However, we find that the DOCP reduces radically even for small displacements below the footprint of the GNP (shaded region) and reaches a minimum of about 0.04 for  $r = 35$  nm. Simultaneously, the relative intensity contribution of dipoles below the center of the GNP is significantly lower than for emitters located below the edge of the GNP. Our findings therefore highlight that the overall farfield polarization of the hybrid system with an ensemble of spatially separated valley excitons can differ significantly from the intuition based on a single rotating electric dipole below the center of the GNP.

In the next section, we aim to provide a quantitative model that describes the observable farfield intensity and polarization of the hybrid system by combining both the effects of excitation and emission. As excitonic emitters in 2D-TMDs are created across the whole excitation area, their distribution needs to be taken into account. We model the emission from such an ensemble of excitons by averaging over a distribution of rotating electric dipoles

$\vec{p}_{K/K'}(x, y)$  for which the local exciton densities  $n_{K/K'}(x, y)$  are proportional to the helical excitation intensities  $I_{\sigma^\pm}^{\parallel}(x, y)$  below the GNP. Note, that for the hybrid system an excitation beam with well-defined  $\sigma^+$  polarization leads to non-zero exciton densities for both valleys  $n_K(x, y)$  and  $n_{K'}(x, y)$ . Simultaneously, an exciton located in the valley K or K' leads to non-zero farfield intensities of both helicities which we denote as  $\mathcal{I}_{\sigma^\pm}^K$  or  $\mathcal{I}_{\sigma^\pm}^{K'}$ , respectively. Then, we describe the helical farfield intensities observed for the hybrid system in wide-field illumination according to Equation 1 and using Gaussian smoothing (where the Gaussian width matches the optical resolution of the experiments, see Methods section for further details). Similarly, we calculate the result for the case of confocal scanning according to Equation 3 where we take into account the dependence of the excitation field on the center position of the focused excitation beam as previously discussed. Ultimately, we compare the calculated farfield DOCP with our measured results for both excitation schemes in Figure 6. Here, we

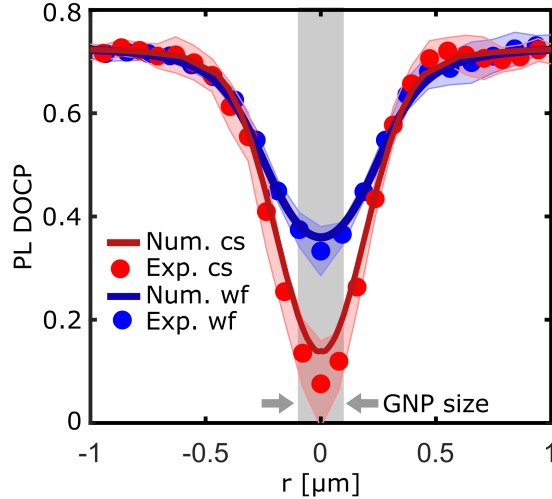


Figure 6: Comparison of the spatial line profiles of the calculated (solid curves) and measured (circles) DOCP as a function of the radial distance  $r$ . Blue and red color corresponds to wide field (wf) and confocal scanning (cs) measurement settings, respectively.

plotted the cross-sections of the measured DOCP of emission from 1L-MoS<sub>2</sub> upon  $\sigma^+$  excitation across the GNPs both for wide-field illumination (blue circles) and confocal scanning (red circles). The cross-sections and error corridors (shaded regions) are obtained by averaging over several GNPs as well as cross-section directions across the GNP. For comparison,

we also plotted the numerical prediction of the farfield DOCP according to Equation 4 for plane wave excitation (blue solid curve) as well as for confocal Gaussian beam excitation (red solid curve). Our numerical calculations closely agrees with the experimental results indicating that the presented model accurately incorporates the dominating physical effects leading to the observed reduction of the DOCP of emission from 1L-MoS<sub>2</sub>.

Interestingly, similar depolarization effects were also described in a very recent theoretical study by Salzwedel et al.<sup>40</sup> for strongly coupled plexcitonic systems on the basis of dipole-dipole interaction. The described systems in their work exhibiting different coupling regimes can serve as further test bed for the validity of our proposed model.

## Conclusion

An accurate theoretical description of the complex emission polarization behaviour of hybrid nanosystems consisting of 2D-TMDs interacting with resonant nanostructures is essential for the design and optimization of nanoscale valleytronic devices. Here we experimentally realized a hybrid model system, which uses a GNP as a probe to systematically investigate the factors determining the emission polarization behaviour of such systems. Specifically, we fabricated CVD-grown 1L-MoS<sub>2</sub> embedded within amorphous silicon oxide thin films being decorated with resonant GNPs and investigated the modification of the DOCP of valley-selective chiral emission from the embedded 1L-MoS<sub>2</sub> by the presence of monodispersed GNPs. We reported a robust and strong reduction in the DOCP as mediated by the GNP and presented a systematic analysis of contributing factors including both excitation and emission effects. While we have found the excitation polarization to be strongly affected at high numerical aperture, the impact can be reduced by employing a wide-field excitation scheme mimicking plane wave excitation. Our respective measurements, however, showed that a significant reduction in the DOCP is still observed beyond the prediction according to the excitation effect alone. Next, we numerically analyzed the impact of the spatial

extend of the emitting 1L-MoS<sub>2</sub> leading to emission contributions from out of the symmetry point of the GNP-on-substrate geometry. Our simulations showed a crucial sensitivity of the farfield DOCP on the emitter position even for emitters located well within the footprint area of the GNP. Ultimately, by averaging contributions from spatially distributed rotating electric dipoles of both helicities weighted by their respective excitation rate, we are able to accurately reproduce the experimentally observed reduction in DOCP by our simulations. This yields a quantitative model for describing the PL emission of two-dimensional TMD-based chiral emitters when in proximity to resonant nanostructures. It further gives insight into the polarization properties of collective emission from ensembles of dipolar emitters when in proximity to all types of nanoresonators as observable by optical farfield techniques. Our present work specifically shows the challenges and limitations for the realization of valleytronic devices on the basis of resonant plasmonic nanostructures.

## Materials and Methods

### CVD growth and embedding of 1L-MoS<sub>2</sub>

Single crystals of 1L-MoS<sub>2</sub> with high optical quality were synthesized on silicon wafers with 300 nm thermal oxide (Sil'tronix, root mean square (RMS) roughness <0.2 nm) by a modified chemical vapor deposition process in which Knudsen cells were employed for the delivery of precursors.<sup>29,30</sup> The grown 1L-MoS<sub>2</sub> single crystals were characterized initially using optical microscopy and Raman spectroscopy and transferred onto a glass substrate using a poly(methyl methacrylate) assisted wet-transfer process.<sup>31</sup> Subsequently, the sample was coated by a thin film of silicon oxide using an adapted physical vapour deposition process<sup>32</sup> (Buhler SyrusPro 1100) using a relatively low deposition rate of 0.5 nm/s and 15 nm target thickness.

## Gold nanoparticle deposition

Initially, the purchased GNP suspension (Merck/Sigma Aldrich, particle size 200 nm) was ultrasonicated for 5 mins and then 20  $\mu\text{L}$  of the suspension were diluted with 60  $\mu\text{L}$  of isopropanol to reach a particle concentration of  $\sim 4.7 \times 10^8$  particles/mL. Subsequently, the diluted suspension was drop-casted onto the sample and spin-coated at 1000 rpm with 500 round/s<sup>2</sup> acceleration for 20 s. This process resulted in a homogeneous distribution of mostly isolated GNPs on the substrate.

## Optical experiments at cryogenic temperatures

Optical experiments were conducted at cryogenic temperatures ( $T = (3.8 \pm 0.1)$  K) using a closed-cycle helium cryostation (Montana Instruments s50) with high numerical aperture optical access (100x/0.9NA) in reflection geometry. For white light spectroscopic measurements, a stabilized tungsten-halogen white light source was used. For photoluminescence spectroscopic measurements, the sample was excited using a 561 nm wavelength continuous-wave diode pumped solid-state laser. For polarization-resolved photoluminescence imaging, the sample was pumped near-resonantly at 633 nm wavelength using a continuous wave helium-neon gas laser. The polarization of the excitation beam was prepared by a linear polarizer and quarter-wave phase plate by monitoring the degree of circular polarization of the collimated excitation beam before entering the objective. In detection, the polarization was analyzed by a combination of super-achromatic quarter-wave phase plate and a linear polarizer. For confocal scanning measurements, the excitation beam was focused to a diffraction limited spot with diameter of  $2r = 2\lambda/(\text{NA} \cdot \pi) \approx 0.45 \mu\text{m}$ . The collected emission was imaged onto an EMCCD camera (Andor iXon 897 Ultra) and integrated over an area of 3x3 pixels (= 48x48  $\mu\text{m}^2$  on camera chip) which relates to an area of 270x270  $\text{nm}^2$  in the conjugated sample plane. For wide-field measurements, an additional lens was introduced to focus the excitation beam onto the back-focal plane of the objective. In all imaging experiments, the collected emission was filtered by a 650 nm longpass filter to block the laser

light collected from the sample in reflection. An additional 660 nm bandpass filter was used to limit the detection to a spectral band as close to the A-excitonic photoluminescence peak as possible.

## Numerical simulations

For the numerical analysis of our hybrid system, we have used the commercial finite-difference time-domain solver (Lumerical FDTD solutions). Perfectly matched layers were applied at each boundary of the simulation area. The nanoparticle was modelled as a gold sphere with a radius of 100 nm lying on a glass that fills the lower halfspace of the FDTD domain. We did not differentiate between the glass substrate and the capping oxide layer, considering both as a homogeneous medium with the refractive index of  $n=1.5$ . The remaining space is filled with air. The optical properties of the materials were taken from the default material database in Lumerical, namely, Handbook of Optical Constants of Solids I - III by E. Palik. Focusing on the excitation aspect, we first computed the in-plane nearfield components  $E_x(x, y)$  and  $E_y(x, y)$  at the position of the monolayer, 15 nm below the nanoparticle. The GNP was illuminated under normal incidence by either a plane wave or a Gaussian beam in a thin lens approximation with  $NA=0.9$ . For both excitation sources we have set circular polarization and center wavelength of 633 nm. The mesh override sections with the mesh size of 5 nm were applied for the areas around the beam focus and nanoparticle to achieve finer resolution. In case of a plane wave, we computed the local valley exciton density as  $n_K(x, y) \propto I_{\sigma^+}^{\parallel}(x, y)$  and  $n_{K'}(x, y) \propto I_{\sigma^-}^{\parallel}(x, y)$ , where  $I_{\sigma^{\pm}}^{\parallel} \propto |E_{\sigma^{\pm}}^{\parallel}|^2 = |E_x \pm iE_y|^2$ . To reproduce the result of confocal scanning we have displaced the focal spot of the Gaussian beam from the nanoparticle center and computed the corresponding  $n_{K/K'}(r, x, y)$  as a function of the displacement distance  $r$ . In the second set of simulations we studied the radiation farfield polarization from a single emitter in 1L-MoS<sub>2</sub> scattered by the GNP. For that we mimicked an emitter from K or K' valley as a pair of perpendicular electric dipoles with 90° or -90° phase shift, respectively. The simulations were performed for different GNP-emitter distances  $r$  as shown in Figure 5a.

High sensitivity of the interaction between the GNP and the dipole emission on the relative distance, yields high sensitivity to the mesh size. Performing the convergence test, we chose 3 nm mesh size around the dipole and the nanoparticle as a good trade-off between the simulation accuracy and computation time. The nearfield was extracted from a horizontal plane right above the nanoparticle and propagated by 1 m to the farfield using the built-in Lumerical functions. The angular filter was applied to the resulting field restricting the accepted emission angles to fit the finite numerical aperture of our objective (NA=0.9). Next, we transformed the filtered field given in spherical coordinates  $\{E_\theta, E_\phi, E_r\}$  into the helical basis  $E_{\sigma^\pm} = E_\theta \pm iE_\phi$ . The corresponding intensities are given by  $\mathcal{I}_{\sigma^\pm}^K(r) = |E_{\sigma^\pm}^K(r)|^2$ , where we have added the valley index  $K$  and dependence on the emitter displacement. Note that from the symmetry considerations, it is sufficient to consider just one valley, because the intensity contributions of the opposite one will be swapped, i.e.  $\mathcal{I}_{\sigma^-}^{K'}(r) = \mathcal{I}_{\sigma^+}^K(r)$  and  $\mathcal{I}_{\sigma^+}^{K'}(r) = \mathcal{I}_{\sigma^-}^K(r)$ . Having quantified both, the excitation and emission processes, we combined them to compare with the experimental results. In case of the widefield experiment, the farfield intensities of  $\sigma^\pm$ -polarized light emitted from every point  $(x, y)$  is given by

$$\mathcal{I}_{\sigma^\pm}(x, y) = n_K(x, y) \cdot \mathcal{I}_{\sigma^\pm}^K(x, y) + n_{K'}(x, y) \cdot \mathcal{I}_{\sigma^\pm}^{K'}(x, y) \quad (1)$$

Next, we took into account the finite resolution of our optical system by applying the Gaussian smoothing  $\tilde{\mathcal{I}}_{\sigma^\pm}(x, y) = \iint G(\xi - x, \eta - y) \mathcal{I}_{\sigma^\pm}(\xi, \eta) d\xi d\eta$ , where

$$G(x, y) = \frac{1}{2\pi\Sigma^2} \exp\left(-\frac{x^2 + y^2}{2\Sigma^2}\right) \quad (2)$$

with  $\Sigma = 174$  nm, as extracted from the widefield experimental data. In case of the confocal scanning configuration, the local exciton densities become depended on the position of the excitation beam relative to the GNP. Therefore, the detected  $\sigma^\pm$  PL intensities at the distance

$r$  from the GNP center becomes

$$\tilde{\mathcal{I}}_{\sigma^{\pm}}(r) \propto \iint n_K(r, \xi, \eta) \cdot \mathcal{I}_{\sigma^{\pm}}^K(\xi, \eta) + n_{K'}(r, \xi, \eta) \cdot \mathcal{I}_{\sigma^{\pm}}^{K'}(\xi, \eta) d\xi d\eta. \quad (3)$$

Note, that here there is no need in applying the Gaussian smoothing because the finite optical resolution is already accounted by integration over the size of the focal spot. Finally, the anticipated DOCP of the PL for both experiments that is shown in Figure 6 was computed as

$$\text{DOCP} = \frac{\tilde{\mathcal{I}}_{\sigma^+} - \tilde{\mathcal{I}}_{\sigma^-}}{\tilde{\mathcal{I}}_{\sigma^+} + \tilde{\mathcal{I}}_{\sigma^-}} \times \langle \text{DOCP}_{\text{PL}}^{\text{bare}} \rangle \quad (4)$$

where  $\langle \text{DOCP}_{\text{PL}}^{\text{bare}} \rangle$  was the averaged experimentally observed DOCP of PL from embedded 1L-MoS<sub>2</sub> without a GNP.

## Acknowledgement

This work was funded by the Deutsche Forschungsgemeinschaft (DFG, German Research Foundataion) – CRC/SFB 1375 NOA "Nonlinear Optics down to Atomic scales" (Project number 398816777), EXC 2051 (Project number 390713860), International Research Training Group 2675 "META-Active" (project number 437527638), and the Emmy Noether Program (Project number STA 1426/2-1). F.E. acknowledges the Bundesministerium für Bildung und Forschung (BMBF, Federal Ministry of Education and Research) support via NanoScopeFutur-2D (Project Number 13XP5053A). M.J.W. acknowledges support by the Australian Research Council (ARC) Centre of Excellence Grant No. CE170100039 and a Schmidt Science Fellowship. We thank M. Younesi and M. Rikers for providing the scanning electron micrographs and J. Gour and R. Schlegel for the preparation and coating of the substrates. We also thank U. Peschel, C. Rockstuhl and I. Fernandez-Corbaton for fruitful discussions on the symmetry properties of chiral emitters. Further, we thank A. Knorr, R. Salzwedel and L. Greten for fruitful discussions on dipole-dipole interactions in

exciton-plasmon based systems.

## Supporting Information Available

Supporting Information Available:

- Full Stokes-polarimetric imaging of cryogenic photoluminescence from 1L-MoS<sub>2</sub> decorated with resonant gold nanoparticles (Figure S1).

## References

- (1) Xu, X.; Yao, W.; Xiao, D.; Heinz, T. F. Spin and pseudospins in layered transition metal dichalcogenides. *Nat. Phys.* **2014**, *10*, 343–350.
- (2) Sun, L.; Wang, C.-Y.; Krasnok, A.; Choi, J.; Shi, J.; Gomez-Diaz, J. S.; Zepeda, A.; Gwo, S.; Shih, C.-K.; Alù, A.; Li, X. Separation of valley excitons in a MoS<sub>2</sub> monolayer using a subwavelength asymmetric groove array. *Nat. Photonics* **2019**, *13*, 180–184.
- (3) Gong, S.-H.; Alpegiani, F.; Sciacca, B.; Garnett, E. C.; Kuipers, L. Nanoscale chiral valley-photon interface through optical spin-orbit coupling. *Science* **2018**, *359*, 443–447.
- (4) Zhang, Y.; Oka, T.; Suzuki, R.; Ye, J.; Iwasa, Y. Electrically switchable chiral light-emitting transistor. *Science* **2014**, *344*, 725–728.
- (5) Hu, G.; Hong, X.; Wang, K.; Wu, J.; Xu, H.-X.; Zhao, W.; Liu, W.; Zhang, S.; Garcia-Vidal, F.; Wang, B.; Lu, P.; Qiu, C.-w. Coherent steering of nonlinear chiral valley photons with a synthetic Au–WS<sub>2</sub> metasurface. *Nat. Photonics* **2019**, *13*, 467–472.
- (6) Jones, A. M.; Yu, H.; Ghimire, N. J.; Wu, S.; Aivazian, G.; Ross, J. S.; Zhao, B.; Yan, J.; Mandrus, D. G.; Xiao, D.; Yao, W.; Xu, X. Optical generation of excitonic valley coherence in monolayer WSe<sub>2</sub>. *Nat. Nanotechnol.* **2013**, *8*, 634–638.

- (7) Xiao, D.; Yao, W.; Niu, Q. Valley-contrasting physics in graphene: magnetic moment and topological transport. *Phys. Rev. Lett.* **2007**, *99*, 236809.
- (8) Schaibley, J. R.; Yu, H.; Clark, G.; Rivera, P.; Ross, J. S.; Seyler, K. L.; Yao, W.; Xu, X. Valleytronics in 2D materials. *Nat. Rev. Mater.* **2016**, *1*, 1–15.
- (9) Xiao, D.; Liu, G.-B.; Feng, W.; Xu, X.; Yao, W. Coupled spin and valley physics in monolayers of MoS<sub>2</sub> and other group-VI dichalcogenides. *Phys. Rev. Lett.* **2012**, *108*, 196802.
- (10) Zeng, H.; Dai, J.; Yao, W.; Xiao, D.; Cui, X. Valley polarization in MoS<sub>2</sub> monolayers by optical pumping. *Nat. Nanotechnol.* **2012**, *7*, 490–493.
- (11) Mak, K. F.; He, K.; Shan, J.; Heinz, T. F. Control of valley polarization in monolayer MoS<sub>2</sub> by optical helicity. *Nat. Nanotechnol.* **2012**, *7*, 494–498.
- (12) Cao, T.; Wang, G.; Han, W.; Ye, H.; Zhu, C.; Shi, J.; Niu, Q.; Tan, P.; Wang, E.; Liu, B.; Feng, J. Valley-selective circular dichroism of monolayer molybdenum disulphide. *Nat. Commun.* **2012**, *3*, 1–5.
- (13) Splendiani, A.; Sun, L.; Zhang, Y.; Li, T.; Kim, J.; Chim, C.-Y.; Galli, G.; Wang, F. Emerging Photoluminescence in Monolayer MoS<sub>2</sub>. *Nano Lett.* **2010**, *10*, 1271–1275.
- (14) Mak, K. F.; Lee, C.; Hone, J.; Shan, J.; Heinz, T. F. Atomically Thin MoS<sub>2</sub>: A New Direct-Gap Semiconductor. *Phys. Rev. Lett.* **2010**, *105*, 136805.
- (15) Kim, S.; Lim, Y.-C.; Kim, R. M.; Froech, J. E.; Tran, T. N.; Nam, K. T.; Aharonovich, I. A single chiral nanoparticle induced valley polarization enhancement. *Small* **2020**, *16*, 2003005.
- (16) Wen, T.; Zhang, W.; Liu, S.; Hu, A.; Zhao, J.; Ye, Y.; Chen, Y.; Qiu, C.-W.; Gong, Q.; Lu, G. Steering valley-polarized emission of monolayer MoS<sub>2</sub> sandwiched in plasmonic antennas. *Sci. Adv.* **2020**, *6*, eaao0019.

- (17) Li, Z.; Liu, C.; Rong, X.; Luo, Y.; Cheng, H.; Zheng, L.; Lin, F.; Shen, B.; Gong, Y.; Zhang, S.; Fang, Z. Tailoring MoS<sub>2</sub> valley-polarized photoluminescence with super chiral near-field. *Adv. Mater.* **2018**, *30*, 1801908.
- (18) Wu, Z.; Li, J.; Zhang, X.; Redwing, J. M.; Zheng, Y. Room-temperature active modulation of valley dynamics in a monolayer semiconductor through chiral Purcell effects. *Adv. Mater.* **2019**, *31*, 1904132.
- (19) Guddala, S.; Bushati, R.; Li, M.; Khanikaev, A.; Menon, V. Valley selective optical control of excitons in 2D semiconductors using a chiral metasurface. *Opt. Mater. Express* **2019**, *9*, 536–543.
- (20) Bucher, T.; Vaskin, A.; Mupparapu, R.; Löchner, F. J. F.; George, A.; Chong, K. E.; Fasold, S.; Neumann, C.; Choi, D. Y.; Eilenberger, F.; Setzpfandt, F.; Kivshar, Y. S.; Pertsch, T.; Turchanin, A.; Staude, I. Tailoring Photoluminescence from MoS<sub>2</sub> Monolayers by Mie-Resonant Metasurfaces. *ACS Photonics* **2019**, *6*, 1002–1009.
- (21) Liu, Y.; Lau, S. C.; Cheng, W.-H.; Johnson, A.; Li, Q.; Simmerman, E.; Karni, O.; Hu, J.; Liu, F.; Brongersma, M. L.; Heinz, T. F.; Dionne, J. A. Controlling Valley-Specific Light Emission from Monolayer MoS<sub>2</sub> with Achiral Dielectric Metasurfaces. *Nano Lett.* **2023**,
- (22) Chervy, T.; Azzini, S.; Lorchat, E.; Wang, S.; Gorodetski, Y.; Hutchison, J. A.; Berciaud, S.; Ebbesen, T. W.; Genet, C. Room temperature chiral coupling of valley excitons with spin-momentum locked surface plasmons. *ACS Photonics* **2018**, *5*, 1281–1287.
- (23) Vadia, S.; Scherzer, J.; Watanabe, K.; Taniguchi, T.; Hoögele, A. Magneto-Optical Chirality in a Coherently Coupled Exciton–Plasmon System. *Nano Lett.* **2023**, *23*, 614–618.
- (24) Yang, Z.; Aghaeimeibodi, S.; Waks, E. Chiral light-matter interactions using spin-valley states in transition metal dichalcogenides. *Opt. Express* **2019**, *27*, 21367–21379.

- (25) Rong, K.; Wang, B.; Reuven, A.; Maguid, E.; Cohn, B.; Kleiner, V.; Katznelson, S.; Koren, E.; Hasman, E. Photonic Rashba effect from quantum emitters mediated by a Berry-phase defective photonic crystal. *Nat. Nanotechnol.* **2020**, *15*, 927–933.
- (26) Wang, J.; Li, H.; Ma, Y.; Zhao, M.; Liu, W.; Wang, B.; Wu, S.; Liu, X.; Shi, L.; Jiang, T.; Zi, J. Routing valley exciton emission of a WS<sub>2</sub> monolayer via delocalized Bloch modes of in-plane inversion-symmetry-broken photonic crystal slabs. *Light Sci. Appl.* **2020**, *9*, 1–8.
- (27) Zheng, L.; Liu, Z.; Liu, D.; Wang, X.; Li, Y.; Jiang, M.; Lin, F.; Zhang, H.; Shen, B.; Zhu, X.; Gong, Y.; Fang, Z. Deep subwavelength control of valley polarized cathodoluminescence in h-BN/WSe<sub>2</sub>/h-BN heterostructure. *Nat. Commun.* **2021**, *12*, 291.
- (28) Zheng, L.; Dang, Z.; Ding, D.; Liu, Z.; Dai, Y.; Lu, J.; Fang, Z. Electron-Induced Chirality-Selective Routing of Valley Photons via Metallic Nanostructure. *Adv. Mater.* **2023**, 2204908.
- (29) George, A.; Neumann, C.; Kaiser, D.; Mupparapu, R.; Lehnert, T.; Hübner, U.; Tang, Z.; Winter, A.; Kaiser, U.; Staude, I.; Turchanin, A. Controlled growth of transition metal dichalcogenide monolayers using Knudsen-type effusion cells for the precursors. *J. Phys. Mater.* **2019**, *2*, 016001.
- (30) Shree, S.; George, A.; Lehnert, T.; Neumann, C.; Benelajla, M.; Robert, C.; Marie, X.; Watanabe, K.; Taniguchi, T.; Kaiser, U.; Urbaszek, B.; Turchanin, A. High optical quality of MoS<sub>2</sub> monolayers grown by chemical vapor deposition. *2D Mater.* **2020**, *7*.
- (31) Winter, A.; George, A.; Neumann, C.; Tang, Z.; Mohn, M. J.; Biskupek, J.; Masurkar, N.; Reddy, A. L. M.; Weimann, T.; Hübner, U.; Kaiser, U.; Turchanin, A. Lateral heterostructures of two-dimensional materials by electron-beam induced stitching. *Carbon* **2018**, *128*, 106 – 116.

- (32) Knopf, H.; Lundt, N.; Bucher, T.; Höfling, S.; Tongay, S.; Taniguchi, T.; Watanabe, K.; Staude, I.; Schulz, U.; Schneider, C.; Eilenberger, F. Integration of atomically thin layers of transition metal dichalcogenides into high-Q, monolithic Bragg-cavities: an experimental platform for the enhancement of the optical interaction in 2D-materials. *Opt. Mater. Express* **2019**, *9*, 598–610.
- (33) Raziman, T.; Godiksen, R. H.; Muller, M. A.; Curto, A. G. Conditions for enhancing chiral nanophotonics near achiral nanoparticles. *ACS Photonics* **2019**, *6*, 2583–2589.
- (34) Raziman, T. V.; Visser, C. P.; Wang, S. J.; Rivas, J. G.; Curto, A. G. Exciton Diffusion and Annihilation in Nanophotonic Purcell Landscapes. *Adv. Opt. Mater.* **2022**, *10*.
- (35) Cameron, R. P.; Barnett, S. M.; Yao, A. M. Optical helicity, optical spin and related quantities in electromagnetic theory. *New J. Phys.* **2012**, *14*.
- (36) Fernandez-Corbaton, I.; Molina-Terriza, G. Role of duality symmetry in transformation optics. *Phys. Rev. B* **2013**, *88*, 085111.
- (37) Lamprianidis, A. G.; Zambrana-Puyalto, X.; Rockstuhl, C.; Fernandez-Corbaton, I. Directional Coupling of Emitters into Waveguides: A Symmetry Perspective. *Laser Photonics Rev.* **2022**, *16*.
- (38) Zambrana-Puyalto, X.; Bonod, N. Tailoring the chirality of light emission with spherical Si-based antennas. *Nanoscale* **2016**, *8*, 10441–10452.
- (39) Eismann, J. S.; Neugebauer, M.; Banzer, P. Exciting a chiral dipole moment in an achiral nanostructure. *Optica* **2018**, *5*, 954–959.
- (40) Salzwedel, R.; Greten, L.; Schmidt, S.; Hughes, S.; Knorr, A.; Selig, M. Spatial Exciton Localization at Interfaces of Metal Nanoparticles and Atomically Thin Semiconductors. *arXiv preprint* **2023**, *arXiv:2305.11099*.

# Supporting Information:

## Influence of resonant plasmonic nanoparticles on optically accessing the valley degree of freedom in 2D semiconductors

Tobias Bucher,<sup>\*,†,‡,¶,△</sup> Zlata Fedorova,<sup>\*,†,‡,¶,△</sup> Mostafa Abasifard,<sup>‡,†,¶</sup>

Rajeshkumar Mupparapu,<sup>‡,¶</sup> Matthias Wurdack,<sup>§,†,‡,¶</sup> Emad Najafidehaghani,<sup>||</sup>

Ziyang Gan,<sup>||</sup> Heiko Knopf,<sup>⊥,‡,¶,#</sup> Antony George,<sup>||,¶</sup> Falk Eilenberger,<sup>⊥,‡,¶,#</sup>

Thomas Pertsch,<sup>‡,¶,⊥,#</sup> Andrey Turchanin,<sup>||,¶,@</sup> and Isabelle Staude<sup>†,‡,¶,#</sup>

<sup>†</sup>*Institute of Solid State Physics, Friedrich Schiller University Jena, 07743 Jena, Germany*

<sup>‡</sup>*Institute of Applied Physics, Friedrich Schiller University Jena, 07745 Jena, Germany*

<sup>¶</sup>*Abbe Center of Photonics, Friedrich Schiller University Jena, 07745 Jena, Germany*

<sup>§</sup>*ARC Centre of Excellence in Future Low-Energy Electronics Technologies and Department of Quantum Science and Technology, Research School of Physics, The Australian National University, Canberra, ACT, 2601, Australia*

<sup>||</sup>*Institute of Physical Chemistry, Friedrich Schiller University Jena, 07743 Jena, Germany*

<sup>⊥</sup>*Fraunhofer Institute for Applied Optics and Precision Engineering IOF, 07745 Jena, Germany*

<sup>#</sup>*Max Planck School of Photonics, Germany*

<sup>@</sup>*Jena Center for Soft Matter (JCSM), 07743 Jena, Germany*

<sup>△</sup>*These authors contributed equally*

E-mail: tobias.bucher@uni-jena.de; zlata.fedorova@uni-jena.de

Number of pages: 3

Number of figures: 1

## Polarization-resolved cryo-PL imaging

We studied the modification of the farfield degree of circular polarization (DOCP) of valley-specific chiral emission from monolayer molybdenum disulphide (1L-MoS<sub>2</sub>) by resonant gold nanoparticles (GNP). In order to infer changes in the degree of polarization from the DOCP alone, linear polarization components must vanish identically. Hence, we have performed full Stokes-polarimetric measurements of the photoluminescence (PL) from 1L-MoS<sub>2</sub> decorated with GNPs by collecting the emission in a helical basis ( $\sigma^\pm$ ) as well as in two linearly polarized basis sets (i.e. horizontal (H)/vertical (V) and diagonal (D)/antidiagonal(A)). The respective measured PL intensities are then denoted by  $\mathcal{I}$  and a subscript indicating the detection polarization, respectively. The normalized Stokes vector  $\vec{\mathbf{S}} = (1, S_1, S_2, S_3)$  is then defined as follows:

$$S_1 = \frac{\mathcal{I}_H - \mathcal{I}_V}{\mathcal{I}_H + \mathcal{I}_V}, \quad S_2 = \frac{\mathcal{I}_D - \mathcal{I}_A}{\mathcal{I}_D + \mathcal{I}_A}, \quad S_3 = \frac{\mathcal{I}_{\sigma^+} - \mathcal{I}_{\sigma^-}}{\mathcal{I}_{\sigma^+} + \mathcal{I}_{\sigma^-}}.$$

Figure 1a shows the measured total emission intensity  $\mathcal{I}_{\text{tot}} = (\mathcal{I}_{\sigma^+} + \mathcal{I}_{\sigma^-})$  of a single crystal of 1L-MoS<sub>2</sub> decorated by GNPs. The inset shows an optical microscopy image of the same sample and in both cases the GNPs are marked by circles, respectively. The GNPs have a negligible effect on the total emission intensity of 1L-MoS<sub>2</sub> as no significant variation in brightness can be associated with the positions of the GNPs. In contrast, when calculating the respective Stokes parameter scans, as shown in Figure 1b for  $\sigma^-$  (top row) and  $\sigma^+$  (bottom row) polarized excitation, we find a clear modulation of the polarization properties of emission from 1L-MoS<sub>2</sub> mediated by the GNPs. For the DOCP or  $S_3$  (right column), we find again a strong reduction as described in the main text. Simultaneously, the linear polarization components of emission from 1L-MoS<sub>2</sub> vanish at the positions of the GNP as

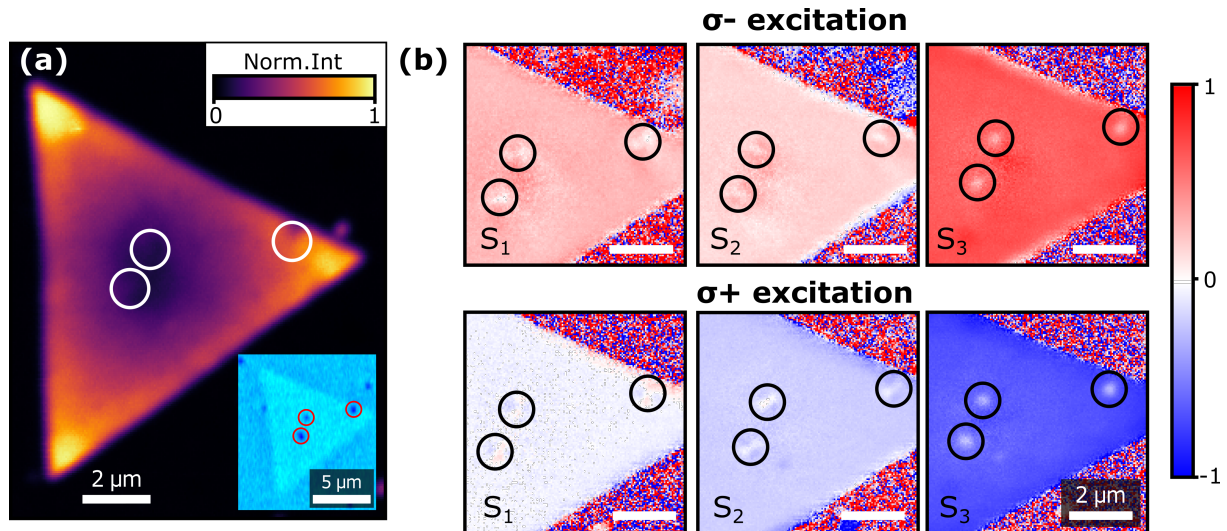


Figure 1: (a) Measured confocal scan of the total emission intensity  $\mathcal{I}_{\text{tot}}$  from embedded 1L-MoS<sub>2</sub> decorated with monodispersed GNPs upon  $\sigma^+$  excitation and collected through a 660 nm bandpass filter. The inset shows an optical microscopy image of the same sample. In both images the position of the GNPs is indicated by circles. (b) Measured confocal scans of the Stokes parameters of emission from the same sample upon  $\sigma^-$  (top row) and  $\sigma^+$  (bottom row) excitation. All scale bars in this subfigure represent  $2 \mu\text{m}$ .

can be seen from the near-zero values of  $S_1$  (left column) and  $S_2$  (middle column). In summary, this shows that the reduction in  $S_3$  is related to a reduction of the overall degree of polarization.